Integration of 2D Hydraulic Model and High-Resolution LiDAR-derived DEM for Floodplain Flow Modeling

Dingtao Shen[a,b,c], Jiechen Wang[a,b,d], Xuejun Cheng[c], Yikang Rui[a,b], Song Ye[c]
[a]Jiangsu Provincial Key Laboratory of Geographic Information Science and Technology, Nanjing, Jiangsu, China
[b]Department of Geographic Information Science, Nanjing University, Nanjing, Jiangsu, China
[c]Changjiang River Scientific Research Institute, Changjiang Water Resources Commission, Wuhan, Hubei, China
[d]Jiangsu Center for Collaborative Innovation in Geographical Information Resource Development and Application, Nanjing, 210023, China

Abstract: The rapid progress of Light Detection And Ranging (LiDAR) technology has made acquirement and application of high-resolution digital elevation model (DEM) data increasingly popular, especially with regards to the study of floodplain flow modeling. High-resolution DEM data include many redundant interpolation points, needs a high amount of calculation, and does not match the size of computational mesh. These disadvantages are a common problem for floodplain flow modeling studies. two-dimensional (2D) hydraulic modeling, a popular method of analyzing floodplain flow, offers high precision of elevation parameterization for computational mesh while ignoring much micro-topographic information of the DEM data itself. We offer a flood simulation method that integrates 2D hydraulic model results and high-resolution DEM data, enabling the calculation of flood water levels in DEM grid cells through local inverse distance weighted interpolation. To get rid of the false inundation areas during interpolation, it employs the run-length encoding method to mark the inundated DEM grid cells and determine the real inundation areas through the run-length boundary tracing technique, which solves the complicated problem of the connectivity between DEM grid cells. We constructed a 2D hydraulic model for the Gongshuangcha detention basin, a flood storage area of Dongting Lake, using our integrated method to simulate the floodplain flow. The results demonstrate that this method can solve DEM associated problems efficiently

and simulate flooding processes with greater accuracy than DEM only simulations.

Key words： 2D hydraulic model, floodplain flow modeling, run-length encoding, LiDAR, digital elevation model

1 Introduction

Floodplain flow simulation is important for forecasting floods and assessing flood disasters. The typical focus of simulation studies is to predict accurate flood inundation extent, depth and duration (Garcia, 2004; Sanyal et al., 2006). In the field of hydraulic calculation, to build a one-dimensional (1D) and two-dimensional (2D) hydraulic models is a common method (Merwade et al., 2008). A 1D hydraulic model is a traditional model, which usually simplifies hydraulic conditions and their physical processes, unable to show and simulate complicated river networks (Gichamo et al., 2012; Samuels, 1990). In comparison, a 2D hydraulic model can simulate the floodplain condition in different periods and places, and calculate inundation extent and depth. Due to these advantages, 2D models are commonly used in floodplain flow studies (Archambeau et al., 2004).

Digital elevation model (DEM) data is the most important data resource for floodplain flow models (Garrote et al., 1995). Its horizontal resolution and vertical elevation precision have much to do with the results calculated by 2D hydraulic modeling (Bates et al, 1996). A few years ago, precise floodplain flow simulation, limited by the accuracy of the DEM data, was the bottleneck problem for 2D hydraulic modeling (Apel et al, 2009). However, the increasing maturity of airborne Light Detection And Ranging (LiDAR) technology has made the acquirement and implement of high-resolution DEM data far easier in recent years. By processing the point cloud data, we can make the spatial resolution of DEM data 1 meter and the vertical error 10-15 centimeters (Haile, 2005). With the high resolution, regional topographic information can be more detailed and micro-topography information of the flattened ditches and balks can

49 be retained, offering the basis for more precise calculation of flood extent and depth (Horritt et al., 2001;
50 Li et al., 2010; Merwade et al., 2008; French, 2003). Many scholars have tried to apply high-resolution
51 LiDAR-derived DEM data to floodplain flow models and analyze the effects of different spatial DEM data
52 resolution on model calculations (Sanders, 2007; Raber et al., 2007). Applying high-resolution DEM data
53 to floodplain flow models has become a common trend in flood studies (Archambeau et al., 2004; Bates
54 et al., 2000).
55 At 1 m horizontal resolution, which is typical of aerial LiDAR surveys, detailed terrain features such as
56 individual buildings can be resolved and researchers have begun to simulate flooding at this scale (Brown
57 et al., 2007; Schubert et al., 2008). Unfortunately, the computational cost of 2D flood simulation at scales
58 approaching 1 m is very high, and it is not unusual to work with study areas of 100 km^2 or more (Sanders
59 et al., 2010). In 2D hydraulic models, finer topographic data are typically re-sampled to coarser meshes
60 (Yu, 2010), and DEM data is used for the valuation assignments of computational mesh nodes. The denser
61 a hydraulic model mesh is, the more time should be spent on the calculation process, which is limited by
62 the processing ability of computers and the complexity of model. The under-utilisation of high-resolution
63 topographic data is due, on one hand, to the exceptionally high computational requirements associated with
64 fine-scale grids; and on the other, to the small time steps required by this type of model in order to achieve
65 computational stability (Yu, 2010).
66 Under mid- or low-resolution DEM, topography appears flatter, allowing the DEM elevation change within
67 a mesh element to be ignored, while hundreds of points of high-resolution LiDAR-derived DEM can keep
68 much micro-topography information that is of high value in calculating inundation extent and depth
69 (Schumann et al., 2008). If DEM data only serves for the valuation assignments of computational mesh
70 nodes, then a lot of elevation point information is largely wasted (Marks et al, 2000). In applying 2D

hydraulic models to the floodplain flow, errors caused by precision differences between the collections of topography data are far greater than those caused by the differences between models (Fewtrell et al., 2011). In recent years, with the development of performance of computers, parallel technology has been employed in calculating hydraulic models (Neal et al., 2010). In stand-alone application environment, the efficiency of multi-core processors-based parallel computation can be several times higher than that of single-core processors (Hervouet, 2000; Pau and Sanders, 2006). However, this improvement on efficiency is still limited for enormous high-resolution DEM, though computer cluster-based parallel computation is able to solve the problems caused by high-resolution DEM data applied in 2-D flood simulation models (Sanders et al., 2010; Yu, 2010). One reason is parallel computation sets a higher request of 2-D hydrologic model programming, because some complex procedures need to be taken into consideration, such as data distribution, computer communication, model scheduling, etc. The other reason is computer cluster-based parallel process has a high requirement on computer software and hardware environment, so many relative researches are limited in laborites and are hard to promote its application. Actually, most of the existing flood modeling packages are designed to work on medium size desktop machines, which does not permit scaling to large size fine resolution domains. In general personal computers, efficient processing of large amounts of DEM data and optimizing the precision of high-resolution vertical and horizontal information is the key to efficient and accurate analysis of large-scale automatic floodplain flow models.

As a result, we put forward a new flood simulation method that integrates a 2D hydraulic model with high-resolution DEM data. Starting with high-resolution DEM data, we constructed a comparatively coarse computational mesh and then constructed a 2D hydraulic model. The results of the 2D hydraulic model were overlaid with the high-resolution DEM data and the flood depth in DEM grid cells was calculated using local inverse distance weighted interpolation. During the process of interpolation, there can be many

93 false flood areas in the DEM grid because parts of the grid cells are interpolated despite not being
94 inundated. To remove false-flooded areas, we marked all of the flooded areas using run-length encoding
95 and then got the real flood extent through run-length boundary tracing technology, a method that proved to
96 save much effort in verifying the connectivity between DEM grid cells. Lastly, we constructed a 2D
97 hydraulic model for the Gongshuangcha detention basin, which is a flood storage area of Dongting Lake,
98 and calculated the inundation extent and depth in different periods using our integrated method. By
99 analyzing and comparing the results, it proves that this method can enhance the accuracy and reliability of
100 floodplain flow modeling.

101 ## 2 Study Area and 2D Hydraulic Model

102 ### 2.1 Study Area and DEM Dataset

103 Dongting Lake (111°40′ ~113°10′ E, 28°30′ ~30°20′ N), with a total area of 18,780 km^2, is located in
104 the middle reaches of Yangtze River (Changjiang River, Figure 1). The districts through which the
105 Dongting Lake flows include Changde, Yiyang, Yueyang, Changsha, Xiangtan, and Zhuzhou in Hunan
106 Province as well as three cities in Jinzhou of Hubei Province. Dongting Lake is surrounded by mountains
107 on three sides and its fountainheads are varied and complicated. It is a centripetal water system fanning out
108 from the center. It only flows into the Yangtze River through Chenglingji of Yueyang (Figure 1).
109 (Insert figure 1 here)
110 In Changjiang River big flood occurred in 1860 and 1870, Ouchi and Songzi burst their banks. Flood
111 flowed into Dongting Lake with large quantity of sediment. Deposition of sediment has caused the rapid
112 growth of the bottomlands and highlands, and some of the watercourses, lakes and bottomlands have been
113 reclaimed. Since then, Dongting Lake has shrank from 4350 km^2 in 1949 to 2625 km^2 in 1995 (measured
114 by Changjiang Water Resources Commission in1995). The total of lake area and spillway area was less
115 than 4000 km^2, about 2/3 of its heyday. Nowadays, Dongting Lake is commonly divided into three parts:

East Dongting Lake, South Dongting Lake and West Dongting Lake, among which West Dongting Lake has the largest water area.

Because of its special location and complex river network system, this area has been frequently prone to flooding. Due to the heavy burden on the masses to deal with floods, lots of labor and money has been spent on dike construction. In order to prevent floods, a total of 266 levees have been built around Dongting Lake areas, and the total length of 5,812 km with the first rank 3,471 km and the second rank 1,509 km. Flooding events in this area have caused significant destruction. The cost of damages following individual events in 1996 and 1998 was 15 and 8.9 billion Yuan, respectively. The pressure of preventing flooding, and the associated damage, has been a major factor affecting healthy economic development and improvement of living standards in Hunan province.

Flood storage and detention areas, which can guarantee the flood control and mitigate flood disaster in key areas, are important components of river flood control system. Basin flood control planning requires to develop regions where necessary conditions are satisfied into flood storage and detention areas, in order to guarantee the flood control in key areas. Measuring overall, planned flood diversion, which guarantee the safety in key areas while bringing loss to some other areas, is reasonable and necessary. At present, there are 98 major flood storage and detention areas in China, which mainly located in middle-lower plain of Changjiang River, Huanghe River, Huaihe River and Haihe River. Gongshuangcha detention basin, one of the largest dry ponds in the Dongting Lake area, is located in the north of Yuanjiang county, facing South Dongting Lake to the east and Chi Mountain to the west with water in between (Figure 2). In total, the detention basin is 293 km^2 in storage area, 121.74 km in levee length, 33.65 m in storage height, has a storage volume of 1.85×10^9 m^3, and is home to 160,000 inhabitants.

(Insert figure 2 here)

We have employed the airborne laser-measuring instrument HARRIER 86i, from German TopoSys

Company, for aerial photography of the Gongshuangcha detention basin from 1st to 8th October, 2010. The digital camera we used was a Trimble Rollei Metric AIC Pro and the inertial navigation system was Applanix POS/AV with a sampling frequency of 200Hz. The laser scanner was Riegl LMS-Q680i, with a maximum pulse rate of 80KHz-400KHz and scanning angle of 45/60.

By processing the point cloud data, we derived a high-resolution DEM of the Gongshuangcha polder detention basin (Figure 3). We checked DEM data quality on plane precision and elevation precision, and the results showed that it could meet the application requirement. DEM plane position was checked by GPS-RTK. After conversion parameters were set and control coordinates were confirmed, ground features' plane coordinates, like corners of buildings, high-tension poles, telecom poles and road edges, were measured. We checked 20 ground feature points, and plane position mean square error is 0.44m. DEM elevation was checked by class 5 leveling. Using annexed leveling line or closed leveling line, we calculated the elevation of check points and compared them with DTM and DEM. We checked 70 elevation points, and elevation mean square error is 0.040m.

The spatial reference is the Gauss-Kruger projection coordinate system with Beijing 1954 datum, and the elevation system is based on the 1985 national elevation standard, of which the lowest elevation is 4.55 meters and highest 45.87 meters. The general landscape shown in the DEM is flat, with much micro topography information of levees, dikes and ridges retained (Figure 3).

(Insert figure 3 here)

2.2 2D Hydraulic Model

In 2008, the Changjiang Water Resources Commission approved a report on the Comprehensive Treatment Planning of Dongting Lake Area (Changjiang Water Resources Commission, 2008). The report highlighted the serious threat of floods, which cause a surplus water volume of 21.8-28 $\times 10^9$ m^3, in the middle and lower reaches of Yangtze River. It also stressed that the effects of the Three Gorges Project, which greatly

influences the conditions for incoming water and sediments, must be taken into consideration. Even though the completion of Three Gorges, and Xiluodu and Xiangjiaba Dams on the Chin-sha River can enhance the flood draining ability around Chenglingji (Figure 1), at the confluence of Dongting Lake and Yangtze River, is the report emphasized the urgent need to construct a 10×10^9 m^3 of diversion storage zone around Chenglingji.

According to the Report on the Feasibility of the Flood Control Project of Qianliang Lake, Gongshuangcha and East Datong Lake of Dongting Lake Areas (Ministry of Water Resources of China, 2009), flood waters from events in 1954, 1966 and 1998, in Chenglingji could have been restricted to safely manageable levels if local detention basins were set up to divert 8,000-12,000 m^3/s of rising waters. For the 1954 flood event, the report shows that the maximum diversion should have been set at 10,000m^3/s, with Qianliang Lake detention basin contributing 4,180m^3/s, Gongshuangcha detention basin 3,630m^3/s, and Datong Lake detention basin 2,190m^3/s, with the corresponding water levels for the dikes set at 33.06m, 33.10m and 33.07m.

According to the standard design of the Gongshuangcha detention basin diversion, we simulated flood flow using a mode controlled by sluice behavior. The resulting hydrograph acted as the input parameter, with flood flow into the sluice conditioned as follows: when water level (H) was below 31.63m, the flow volume into the sluice was 3,630m^3/s; when H was 31.63-32.60m, flow volume was 3,050 m^3/s; when H was 32.60-33.65m, another flow diversion exit was opened.

The flood routing model employed 2D unsteady shallow water equations to describe the water flow, used FVM and Riemann approximate solvers to solve the coupled equations, and simulated flood routing inside the detention basin. We used non-structural discrete mesh to represent the computational zone based on the landscape of the area and the location of water conservancy projects. Then to make ensure accurate

conservation, we used FVM to decide bulk, momentum and the equilibrium of density for each mesh element in different periods. To ensure precision, we used Riemann approximate solver to calculate the bulk and normal numerical flux of the momentum between the mesh elements. The model solves the equations through FVM discretions and converting 2D problems into series of 1D problems with the help of the coordinate rotation of fluxes. The basic principles are as follows.

(1) Basic Control Equation. The Vector Expression of Conservative 2D Shallow Water Equation:

$$\frac{\partial q}{\partial t}+\frac{\partial f(q)}{\partial x}+\frac{\partial g(q)}{\partial y}=b(q) \qquad (1)$$

In this expression the conservative vector q = [h, hu, hv]T, the flux vector of X-direction $f(q)$ = [hu, hu^2+gh^2/2, huv]T, and the flux vector of Y-direction $g(q)$ = [hv, huv, hv^2+gh^2/2]T. h is height, u and v correspondingly mean the average uniform flux of X- and Y- directions, g is the gravity and the source term $b(q)$ is:

$$b(q)=[q_w, gh(s_{0x}-s_{fx})+q_w u, gh(s_{0y}-s_{fy})] \qquad (2)$$

In this expression, S_{0x} and S_{fx} are the river slope and friction slope on X-direction; S_{0y} and S_{fy} are the river slope and friction slope on Y-direction; q_w is the net depth of water in each time unit. The friction slope could be calculated through Manning Formula.

(2) The Discretization of Equations. Calculate basic FVM equation through discretization on any unit of Ω by divergence principle.

$$\iint_{\Omega} q_t d\omega=-\int_{\partial\Omega} F(q)\cdot n dL+\iint_{\Omega} b(q) d\omega \qquad (3)$$

In this expression, n is the normal numerical flux outside of unit $\partial\Omega$, $d\omega$ and dL are surface integration and line integration, and $F(q)$ n is the normal numerical flux, where $F(q)$ = [f(q), g(q)]^T. These equations demonstrate that the solution could convert 2D problems into series of local 1D problems.

(3) Boundary Condition. The model sets five kinds of flow boundaries: earth boundary, the outer boundary of slow and rushing flow, the inner boundary, flowing boundary of no-water and water exchange unit and tributary boundary of wetland.

(4) The solution to the equation. The equations, which are explicit finite schemes can be solved through interactive method over time.

The computational mesh of the 2D hydraulic model of Gongshuangcha detention basin (Figure 4) is constructed by a non-structural triangular mesh in which there are 83,378 triangles, each of whose side length is between 100m-150m. The model mesh densifies the main levees with triangulars (each side length is between 60m-80m). With the 1-m-resolution DEM data, we get the elevation value of the mesh node and triangles centre points through nearest interpolation and make the value as the initial condition. The model computes the water level of each triangular mesh's central point every 10 minutes. Finally, it simulates 50 periods' inundation processes (8 hours and 20 minutes in total).

(Insert figure 4 here)

3 Methodology

3.1 Overview

The inundation process is very hard to simulate because it varies over time. For each particular time, there is a winding curved water surface. If we overlay the water surface calculated from a certain time with DEM data, then the inundation area is where the water level is greater than topography elevation. As a result, the key point of flood inundation simulation is to calculate water surface height. According to different inundation models, there are three main computation methods: the flat-water model, 1D hydraulic model and the 2D hydraulic model.

The flat-water model assumes that water level is a horizontal plane. In this method, flooding of cities or coastal areas due to storms or rise of water level can be modeled relatively easily (Demirkesen et al, 2007;

228 Wang et al., 2002; John, 2001). Two common methods are used to decide the inundation extent from DEM:
229 the bathtub approach (Moorhead and Brinson 1995; Titus and Richman 2001) and the seeded region
230 growing approach (Poulter et al., 2008).
231 The Bathtub approach, also called “zero-side rule”, does not take connectivity issue of DEM grid cells into
232 consideration. All the DEM grid cells whose elevation values are below floodwater level are regarded as
233 flooded areas, and the inundation extent consisted of DEM grid coverage, as expressed by Equation 4:

234 $$Flood\ Extent = \{cell: Z_{cell} < Z_{water\ level},\ cell \in Q\} \quad (4)$$

235 where Z_{cell} is the elevation value of DEM grid cell, $Z_{water\ level}$ fixes the level of floodwater, and Q is the
236 assemblage of DEM grid cells.
237 The seeded region growing approach considers DEM grid cell connectivity. The premise of the inundation
238 of DEM grid cells is that the elevation is below the floodwater level and also next to an inundated DEM
239 grid cell. This approach usually chooses some inundated DEM grid cells as seeds and then simulates the
240 flood diffusion by four-side or eight-side rule. The flood extent consists of the coverage of DEM grid, as
241 expressed by Equation 5:

242 $$Flood\ Extent = \{cell: Z_{cell} < Z_{water\ level} \wedge cell\ connect\ with\ point,\ cell \in Q,\ point \in P,\ P \subseteq Q\} \quad (5)$$

243 where Z_{cell} is the elevation value of DEM grid cell, $Z_{water\ level}$ fixes the level of floodwater, *point* is a real
244 inundated seeded grid cell, Q is the assemblage of DEM grid cells, and P is the assemblage of inundated
245 seeded grid cells among the whole DEM grid.
246 1D hydraulic models can divide watercourses into cross sections and get the information of the water level
247 and flow of cross sections for unique time points. Because 1D hydraulic models do not involve detailed
248 topography information, it is hard to extract the parameters of inundation simply through calculating the
249 water level of cross sections. A good way to solve the problem is to calculate the actual depth of every

DEM grid cell and then decide the inundation extent (Tate et al., 1999). Similar to the flat-water model, this model has to solve the connectivity issue during the process of performing interpolation on DEM grid cells that are in-between cross sections. Interpolated cells that are not inundated cannot be connected with the real inundated DEM grid cells of the watercourse. Previous work suggests that this issue can be solved using methods such as geostatistical interpolation routines (March et al., 1990, Sorensen et al., 1996), neighbourhood analysis (Jonge et al., 1996), and cost distance mapping (Werner, 2001).

2D hydraulic models, two common modeling computational meshes are regular tessellation and triangular irregular net-TIN. Triangular irregular net-TIN is more popular has an advantage on showing the topographic reliefs because it can improve the density of some areas of the triangular mesh to adjust to the changes of terrain and provide a better realization of topographic relief (Casas et al., 2006). According to different solutions of hydraulic computational equations, this model can get the water level of every mesh node or the central point of mesh element at different time. As the hydraulic computation mesh is an approximate expression of digital terrain, flood water level and inundation depth of each mesh unit can be derived after calculating every water level value. Floodplain extent and inundation depth can be calculated directly if there is low demand for result precision (Marks et al, 2000).

3.2 Local Inverse Distance Weighted Interpolation

With high-resolution DEM data, it is not precise to give the floodwater level for the whole DEM grid cells in the mesh element directly because the actual elevation value of each cell in the DEM grid is different. One reasonable way is to calculate water level of every DEM grid cell through spatial interpolation technology like 1D hydraulic modeling. There are some common spatial discrete water level point-based interpolation methods for flood water level including inverse distance weighted interpolation (Werner, 2001; Moore, 2011) and linear interpolation(Apel et al, 2009). Some of the discrete points interpolation based on

natural neighbours, because of its comparatively better performance in evaluating terrain changes, also have quite obvious advantages in flood level interpolation(Sibson, 1981; Belikov and Semenov, 1997; Sukumar et al., 2001). Inverse distance weighted interpolation is a comparatively simple way to get the spatial interpolation data, which can interpolate the value of unknown points with given the location and value of known points. The common equation of inverse distance weighted interpolation is as follows:

$$z(x_j) = \frac{\sum_{i=1}^{n} z(x_i) \times d_{ij}^{-r}}{\sum_{i=1}^{n} d_{ij}^{-r}} \qquad (6)$$

In this equation, x_j stands for the unknown points that need to be interpolated, $z(x_i)$ is the elevation of $NO.i$ known point x_i, d_{ij}^{-r} is the distance between each pair of unknown and known points. Usually, r is set as 2 for spatial data interpolation. In a high-resolution DEM, we could get a water level value for each central point of every DEM grid cell through interpolation based on the equation above, and compare the water level value with the elevation value of DEM grid cell. If the water level value is higher than that of the DEM grid cell, it means this grid cell is inundated. The inundation depth of the DEM grid cell is the water level value minus the grid cell elevation value.

(Insert figure 5 here)

It is of high importance to choose computational mesh nodes as the known interpolated points for the water level interpolation of DEM grid cells because it is improper to get all the nodes in a hydraulic model involved in water level interpolation when tens or even hundreds of thousands computational mesh nodes are involved. Figure 5 shows a non-structural modeling computation mesh (TIN). The computational water level value of the model could be located on the central point of every triangle (as C1-C13 shows) or on the node of the triangle (as P1-P12 shows) according to different solutions of the equation. For the cell located at row I and column J of the DEM grid, we can decide the location of the cell by the spatial coordinate of

293 the central point. If a DEM grid cell (the black square) is inside △P1P2P3, the following methods can be
294 used to choose the nodes of water level interpolation:
295 (1) The case is that the computational water level value locates at the center of the triangle. Firstly, get the
296 coordinate and its water level value of the central point C13 of △P1P2P3. Then search all the triangles that
297 share the nodes P1, P2 and P3 with △P1P2P3, and calculate the coordinate of the central points of these
298 triangles (C1-C12) and their water level values. The Equation of water level of grid cell at row I and
299 column J is expressed as:

300 $$z(x)=\frac{\sum_{i=1}^{13} z(C_i)\times d_{ix}^{-2}}{\sum_{i=1}^{13} d_{ix}^{-2}} \qquad (7)$$

301 In this equation, *x* stands for the central point which is located at row I and column J of DEM grid, z(C_i) is
302 the water level value of *NO.i* known point, C is the central point of the triangle, and the distance between
303 each pair of *NO.i* known point and grid node x is represented by d_{ix} raised to the power r, which is set as 2
304 for spatial data interpolation.
305 (2) The case is that the computational water level value is located at the node. Firstly, get the coordinate
306 and its water level value of the nodes P1, P2 and P3 of △P1P2P3. Then search all the triangles that share
307 the nodes P1, P2 and P3 with △P1P2P3, and calculate the coordinate of all the nodes of these triangles
308 (P4-P12) and their water level values. The Equation of water level of grid cell at row I and column J is
309 expressed as:

310 $$z(x)=\frac{\sum_{i=1}^{12} z(P_i)\times d_{ix}^{-2}}{\sum_{i=1}^{12} d_{ix}^{-2}} \qquad (8)$$

311 In this equation, *x* stands for the central point which is located at row I and column J of DEM grid, *z(x)* is

312 the water level elevation of *x,* z(P_i) is the water level value of *NO.i* known point, P is the vertex of the
313 triangle, and the distance between each pair of *NO.i* known point and grid node x is represented by d_{ix}
314 raised to the power r, which is set as 2 for spatial data interpolation.
315 The method mentioned above can interpolate the inside of actual flood extent. As the water level elevation
316 of all the known points that are calculated in local areas are equal to the DEM grid cell elevation, DEM grid
317 cells that are not inundated can be decided without interpolating, which reduces the amount of calculation.
318 The method can also be employed for other kinds of computational grid, like a quadrilateral grid.

319 **3.3 Inundated Grid Cells Storing and Labelling**

320 Because much micro-topography information is retained in high-resolution LiDAR-derived DEM data,
321 many man-made surface features become a part of the DEM, like dams and trenches and the surfaces of
322 ponds that cannot be represented on some mid- or low-resolution DEM (Figure 6). Suppose that there is a
323 pond surrounded by levees in four-sides. Although the pond becomes inundated during the process of
324 interpolation, it is not actually flooded because the levees do not suffer from the flood. This is a typical
325 false inundation area. Another issue is ringed mountains, although the elevation of some areas among
326 mountains is lower than flood water level, these areas are not flooded because of the protection of the
327 mountains.
328 (Insert figure 6 here)
329 To solve the problem, calculated the actual flood extent based on the connectivity principle. However, some
330 judgment methods to solve the connectivity problem of flat-water and 1D hydraulic models are based on
331 the entire DEM. These methods cannot be applied to high-resolution DEM data because of the prohibitive
332 DEM size and the computation capability required. Using the seeded region growing method, a difficult
333 amount of data to process, 8.36GB (220,000 Rows × 51,000 Columns × 8 Bytes ≈ 8.36GB), stored in the
334 memory of a computer is required when dealing with the DEM data of our study area. On the other hand,

335 the seeded region growing method is a recursive algorithm with low efficiency of computation. Problems
336 like recursion might be too deep when dealing with a large amount of data and the stack of a computer is
337 overflowed to the extent that computation failures can occur. As a result, it is not an idealistic way to
338 employ such neighborhood analysis methods to solve DEM grid connectivity problems when facing a large
339 scale, high resolution, and an enormous amount of DEM data.
340 Due to a large amount of DEM data, which is hard to read for one time, it is better to divide the data into
341 strips to read. As Figure 7 shows, DEM data is divided into 5 strips spatially with each being read at one
342 time. The results of water level interpolations are concurrently stored on a raster file with a null value grid
343 equal to the source DEM data. Every time individual strip water level is interpolated, the result is stored on
344 a corresponding raster file. To process large volumes of DEM data, the memory that has been taken up by
345 the previous strip is released before next data strip is read.
346 (Insert figure 7 here)
347 There are two states for every grid cell during DEM grid interpolation: un-inundated and
348 might-be-inundated. This is typical binary raster data. If we perform run-length compressed encoding to the
349 sequential might-be-inundated DEM grid cells in raster rows, we can mark all the might-be-inundated cells
350 and store them in memory. Run-length encoding is a typical compressed method for raster data (Chang et
351 al., 2006; He et al., 2011), which encodes the cells with same value in compression. Every run-length only
352 needs to mark the cells where it starts across where it ends, which reduces the storage of data remarkably.
353 Figure 7 shows the run-length compressed encoding of the might-be-inundated DEM grid cells. Area A in
354 blue is the real inundation extent where there are three islands. There is a false inundation area inside the
355 middle island. The following are the equations of run-length data and run-length list on the raster:
356 $$Run\ Length\ Dataset = \{RLList: RLList = (RowIndex, RLNum, RLS)\} \quad (9)$$
357 $$RLS = \{RL:RL=(RLIndex, StartCol, EndCol)\} \quad (10)$$

As Equation 9 shows, run-length data is mainly comprised of the RL Lists on every raster row. The list means the run-lengths of current raster rows, on which there are RowIndex, RLNum and RLS. In Equation 10, RLS consists of all the run-lengths on one raster row, and each run-length carries its RLIndex, StartCol and EndCol.

3.4 Connectivity Detection Principle

After finishing DEM grid water level interpolation and storage of run-length compressed encoding of inundated cells, the connectivity issue of DEM grid cells can be solved by run-length boundary tracing technology (Quek, 2000). To prove the connectivity of two inundated cells of DEM randomly, only the judgment of connectivity of the corresponding run-lengths is needed. Both the right and left borders of a run-length are traced vertically and horizontally. if the two run-lengths are connected, then their borders can be traced to form a closed loop.

(Insert figure 8 here)

As Figure 8 shows, three inundated cells in a raster field are marked in purple. To prove the connectivity between Inundated cell 1 and Inundated cell 3 the run-length of Inundated cell 1 (the first run-length on the raster row) and Inundated cell 3 (the fourth run-length on the raster row) must be found. If these run-lengths are connected the boundary trace from the left of the run-length of 1 (as is shown from the graph) to the right of 3 as long as it is on the left of 1.

If the boundary trace from the left of the run-length of Inundated cell 1 meets the right of the run-length of Inundated cell 3, then the cells can be connected. Likewise, if the run-length of 1 and the run-length of 2 cannot meet each other by boundary tracing, then they are not connected. Based on mutual exclusion, as long as we know that 1 is the real inundation area, all the areas connected to 1 are real inundation areas, and all the areas connected to 2 are false inundation areas. As a result, the run-lengths have already carried the information of connectivity between inundation grid cells and the connectivity problem could be worked

out through boundary tracing. Compared with the seeded region growing method, this method only need search along the run-length borders to prove the connectivity between cells, allowing for far faster computation speed.

3.5 False Inundation Area Exclusion

Based on the method mentioned above, we can remove false inundation areas from run-length boundary tracing and get the map of flood extent and depth. Figure 9-(1) shows the run-length boundary tracing and flood extent, in which run-lengths is marked in red rectangles. DEM data only includes 25 raster rows, the model computation mesh is only expressed by four triangles, and the run-lengths are simplified. The water level value of the central point of the mesh element is calculated by model computation, so we can calculate the flood extent by tracing the boundaries of the run-lengths, which can be searched on the central points of the whole computational model elements.

(Insert figure 9 here)

Take Figure 9-(1) for example, the inundated central point of △ABC can be found on the first run-length on the eleventh raster through its spatial coordinate. From the left of this run-length, the outer boundary of flood extent can be traced (Figure 9-(1)) and from the right of this run-length, one of the inner boundaries of flood extent can be traced (Figure 9-(2)). The outer boundary of the entire flood extent can be also traced through boundary tracing of the run-length that can be searched from the central point of △CDE (the 9^{th} row). To avoid repetition of run-length tracing, and to mark real inundated run-lengths, it is important to set two labels along two sides of the run-length to indicate whether a run-length has previously been traced. Run-lengths are marked as traced once one of the sides is traced. Boundary tracing of the run-length where the central point of △CDE is located is not performed when the run-length of the central point of △ABC has been traced.

After boundary tracing through all the central points of the inundated computational mesh elements, some

of the run-lengths are only traced by one side, like rows 5-8 and 12-17 in Figure 9-(2). They are located at the islands of the flood extent. Traverse through the run-lengths to search the islands of the flood extent. Once one side of a run-length is traced while the other not, all the islands can be found by tracing from the untraced side and performing boundary tracing (Figure 9-(3)). At this time, there are only two kinds of run-length. One is that each side of the run-length is traced, and the other is that neither side of the run-length is traced. The extent of untraced run-lengths shows false inundation areas. Therefore, the false inundation extent can be automatically removed by boundary tracing. Meanwhile, flood extent and depth can be interpolated automatically from the traced run-length (Figure 9-(4)).

4 Results and Discussion

4.1 Flood Inundation Results

According to the principle mentioned above, we get the 50 periods' flood extent and depth of Gongshuangcha detention basin of Dongting Lake area. Figure 10 (NO.10, No.30 and NO.50 periods) shows the comparison between the result from the 2D hydraulic model and the result of the method mentioned above. The resolution of the 2D hydraulic model mesh is above 100 meter, whereas this method mentioned above interpolates the water level through 1m high-resolution DEM. As a result, although the whole flood extents differ little, the distributions of flood depth are very different from each other. The maximum inundation depth calculated by our method is 70cm higher than that of the 2D hydraulic model.

(Insert figure 10 here)

Figure 11 shows the No.50 period of process of inundation and its regional enlarged view. Figure 11-(1) is the high-resolution aerial remote sensing image taken by an airborne LiDAR system, whose spatial resolution is 0.3m. From this image we can see the distribution of farmlands, roads, channels, levees and houses clearly, among which the houses are constructed along rivers and levees. Figure 11-(2) and 11-(3) are the 2D hydraulic model and our methods regional enlarged view of the inundation area. The mesh

resolution of a 2D hydraulic model is coarser compared with the geographic features of roads and houses, so the result can only prove that the flood depth of that area is lower while the ponds on the left of the image cannot be expressed. It also cannot show the flood condition of every house. However, with the help of our method, important geographic features can be clearly expressed. From Figure11-(3) it is obvious that not only the flood condition of channels, ponds and levees are clearly expressed, but also the difference of flood depths between ridges of paddy fields. In Figure11-(3) there are three linear areas which are not inundated. From Figure11-(4) we can tell that those are levee crests on which houses and roads are being constructed.

(Insert figure 11 here)

4.2 Inundation Area and Volume statistics

We compare the flood extents calculated from the 2D hydraulic model and the method mentioned above for 50 different periods. In the 2D hydraulic model, the flood extent is calculated by adding up every inundated triangle's area from the hydraulic computational mesh, while in the method of this paper, the flood extent is calculated by summing every real inundated cell area based on of 1-m-resolution DEM data. It can be expected that the flood extent calculated from the 2D hydraulic model is larger than that from the method of this paper (Figure 12). The 2D hydraulic model cannot take the micro-topography information into full consideration, and many details cannot be shown on the model computational mesh, like some secondary levees, ponds and steep slopes. We get a smaller area result because we can get rid of the parts in the computational mesh whose elevation values are higher than the interpolated water levels.

Among the 50 periods, the flood area calculated by a 2D hydraulic model surpasses that of our method by 5%-17%.The exceeding flood area is getting larger. In the 50^{th} period, the flood area of the 2D hydraulic model is 6 square kilometers larger than that of this paper's method.

(Insert figure 12 here)

As for the inundation volume, the result calculated by the 2D hydraulic model is smaller than that calculated by our method (Figure 13). According to the previous graphs the maximum inundation depth and the regional inundation depth calculated by our method are larger than the 2D hydraulic model, which means that the whole digital topography could be higher if we employ model computational mesh to express the topography directly. The difference of results is from 3% to 8%, and in the 50th time-period, the inundation volume difference is $9.689 \times 10^6 m^3$.

(Insert figure 13 here)

4.3 Discussion

The precision of digital topography is a key factor for flood simulation and analysis. Spatial resolution and Vertical precision are both important for mapping of flood extent and depth. Employing high-resolution topography data can make up for the errors of a 2D hydraulic model.

With high-resolution topography data, flood simulation can be analyzed from the basis of topography to geographic elements because some of the most important micro-topography information is accounted for by digital topography data, especially that of levees, ponds and man-made architectures. Once we take the factors from the flood extent and depth map into consideration, we can get the results with more precision. However, a coin has two sides. With more man-made architectures using high-resolution digital topography, new problems might occur because some false topography information might be involved. For example, the airborne LiDAR point cloud data could not be distinguished from the data of channels, bridges over reaches or viaducts over roads. The redundant information could affect the simulation and analysis of floodplain flow model. To remove redundant information, much later treatments are needed and might complicate the situation.

5 Conclusion

With the help of photogrammetry and remote sensing technology, we can survey the digital terrain of a

large scale of reaches with high precision. Problems like a loss of topography materials and lack of data accuracy are being gradually solved, allowing for progressively greater precision for analysis and assessment of flood disaster risks. The rapid development of LiDAR technology has especially promoted the acquirement and update of digital terrain data and shown its great potential for relevant study and application to flood disaster studies.

To employ LiDAR-derived DEM to simulate flood routing directly is not realistic because of the complexity of calculation of a hydraulic model with a prohibitively high-resolution mesh. Thus, we need to construct a relative coarse model mesh on the basis of high-resolution digital topography. However, lots of micro-topography information of high-resolution DEM has been ignored when we deal with flood parameters, which have direct relation to inundation extent and depth. As a result, this paper hopes to offer a method, which integrates a 2D hydraulic model with high-resolution LiDAR-derived DEM to simulate floodplain flow. This method can calculate the flood extent and depth with much more precision during floodplain flow modeling. With this kind of digital topography and data of residential houses and public infrastructure, the floods caused by different reasons can be analyzed in greater detail. These factors demonstrate the great application potential of our method for predictive flood simulation and accurate assessment of potential loss from flooding events.

Acknowledgements

This work was supported by the fundamental research funds for central public welfare research institutes (Grant No.CKSF2013016/KJ, CKSF2014031/KJ), the National Natural Science Foundation of China (Grant No. 51409021, 41301435), the National Twelfth Five-Year Plan for Science & Technology Support Program(Grant No. 2012BAK10B04), and the Program for New Century Excellent Talents in University (NCET-13-0280).

References:

Apel, H., Aronica, G.T., Kreibich, H., Thieken, A.H.. Flood risk analyses-how detailed do we need to be?[J]. Natural Hazards, 2009,49(1), 79-98.

Archambeau, P., Dewals, B., Erpicum, S., Detrembleur, S., Pirotton, M., 2004. New trends in flood risk analysis: working with 2D flow model, laser DEM and a GIS environment, 2004.

Bates P.D., Anderson M.G., 1996. A preliminary investigation into the impact of initial conditions on flood inundation predictions using a time/space distributed sensitivity analysis[J]. Catena, 26, 115-134.

Bates, P.D., De Roo., A.P.J., 2000. A simple raster-based model for flood inundation simulation[J]. Journal of Hydrology, 236, 54-77.

Belikov V.V., Semenov A.Y., 1997. New NonSibson Interpolation on Arbitrary System of Points in Euclidean Space. Proceedings of 15th World Congress on Scientific Computation Modeling and Applied Mathematics. Berlin August 1997.

Belikov V.V., Semenov A.Y., 2000. Non-Sibsonian interpolation on arbitrary system of points in Euclidean space and adaptive isolines generation[J]. Applied Numerical Mathematics, 32:371-387.

Brown, J.D., Spencer T., Moeller I., 2007. Modeling storm surge flooding of an urban area with particular reference to modeling uncertainties: a case study of Canvey Island, United Kingdom[J]. Water Resour Res, 43:W06402.

Casas, A., Benito, G., Thorndycraft, V.R., Rico, M., 2006. The topographic data source of digital terrain models as a key element in the accuracy of hydraulic flood modelling[J]. Earth Surfaces Processes and Landforms, 31(4), 444-456.

Chang, C.C., Lin, C.Y., Wang, Y.Z., 2006. New image steganographic methods using run-length approach[J]. Information Science, 176(22), 3393-3408.

Chen, J., Hill, A.A., Urbano, L.D., 2009. A GIS-based model for urban flood inundation[J]. Journal of Hydrology, 373, 184-192.

CWRC, 2008. Comprehensive Treatment Planning of Dongting Lake Area, Changjiang Water Resources Commission, China.

517 Demirkesen, A.C., Evrendilek, F., Berberoglu, S., Kilic, S., 2007. Coastal Flood Risk Analysis Using Landsat-7 ETM+
518 Imagery and SRTM DEM: A Case Study of Izmir, Turkey[J]. Environmental Monitoring and Assessment, 131(1-3), 293-300.
519 Fewtrell, T.J., Duncan, A., Sampson, C.C., Neal, J.C., Bates, P.D., 2011. Benchmarking urban flood models of varying
520 complexity and scale using high resolution terrestrial LiDAR data[J]. Physics and Chemistry of the Earth, 36, 281-291.
521 French, J.R., 2003. AIRBORNE LIDAR IN SUPPORT OF GEOMORPHOLOGICAL AND HYDRAULIC MODELLING[J].
522 Earth Surface Processes and Landforms, 28, 321-335.
523 Garcia, S.G., 2004. GRASS GIS-embedded Decision Support Framework for Flood Simulation and Forecasting[J].
524 Transactions in GIS, 8(2), 245-254.
525 Garrote, L., Bras, R.L.. A distributed model for real-time flood forecasting using digital elevation models[J]. Journal of
526 Hydrology, 1995,167, 279-306.
527 Gichamo, T.Z., Popescu, I., Jonoski, A., Solomatine, D., 2012. River Cross-section extraction from the ASTER global DEM
528 for flood modeling[J]. Environmental Modelling & Software, 31, 37-46.
529 Haile, A.T.. Integrating Hydrodynamic Models and High Resolution DEM(LiDAR) For Flood Modelling. Master's Degree
530 Paper. International Institute for Geo-Information Science and Earth Observation Enschede, The Netherlands, 2005.
531 He, Z., Sun, W., Lu, W., Lu, H., 2011. Digital image splicing detection based on approximate run length[J]. Pattern
532 Recognition Letters, 32(12), 1591-1597.
533 Hervouet, J., 2000. A high resolution 2-D dam-break model using parallelization. Hydrological Processes 14 (13),
534 2211–2230.
535 Horritt M.S., Bates P.D.. Effects of spatial resolution on a raster based model of flood flow[J]. Journal of Hydrology,
536 2001,253, 239-249.
537 John Dobosiewicz, 2001. Application of Digital Elevation Models and Geographic Information Systems to Coastal Flood
538 Studies along the Shoreline of Raritan Bay, New Jersey[J]. Environmental Geoscience,8(1), 11-20.

539 Jonge, T. de, Kok, M., Hogeweg, M., 1996. Modelling floods and damage assessment using GIS, in HydroGIS96:
540 Application of Geographical Information Systems in Hydrology and Water Research. Management and Planning Proceedings
541 of the Vienna Conference, 4-1996, IAHS Publ, 235, 299-306.
542 Li, J., Wong, D.W.S.. Effects of DEM sources on hydrologic application[J]. Computers, Environment and Urban Systems,
543 2010,34, 251-261.
544 March, C., Lessard, G., Gharbi, B.El.. Kriging technique for river flood representation, Journal of Hydraulic Research,
545 1990,28(5), 629-643.
546 Marks, K., Bates, P., 2000. Integration of high-resolution topographic data with floodplain flow models[J].
547 HYDROLOGICAL PROCESS, 14, 2109-2122.
548 Merwade, V., Cook, A., Coonrod, J., 2008,GIS techniques for creating river terrain models for hydrodynamic modeling and
549 flood inundation mapping[J]. Environmental Modelling & Software, 23:1300-1311.
550 Moore, M.R., 2011. Development of a high-resolution 1D/2D coupled flood simulation of Charles City, Iowa. MS (Master of
551 Science) thesis, University of Iowa, 49-68.
552 Moorhead, K.K., Brinson, M.M., 1995. Response of wetlands to rising sea level in the lower coastal plain of North
553 Carolina[J]. Ecological Applications, 5, 261-271.
554 MWR, 2009. Report on the Feasibility of the Flood Control Project of Qianliang Lake, Gongshuangcha and East Datong
555 Lake of Dongting Lake Areas, Ministry of Water Resources, China.
556 Neal, J.C., Fewtrell, T.J., Bates, P.D., Wright, N.G., 2010. A comparison of three parallelisation methods for 2D flood
557 inundation models[J]. Environmental Modelling & Software, 25:398-411.
558 Pau, J.C., Sanders, B.F., 2006. Performance of parallel implementations of an explicit finite-volume shallow-water model[J].
559 Journal of Computing in Civil Engineering, 20 (2), 99–110.
560 Poulter, B., Halpin, P.N., 2008. Raster modelling of coastal flooding from sea-level rise[J]. International Journal of

561 Geographical Information Science, 22(2), 167-182.

562 Quek, F.K.H., 2000. An algorithm for the rapid computation of boundaries of run-length encoded regions[J]. Pattern

563 Recognition. 2000, 33(10), 1637-1649.

564 Raber, G.T., Jensen, J.R., Hodgson, M.E., Tullis, J.A., Davis, B.A., Berglund, J., 2007. Impact of Lidar Nominal Post-spacing

565 on DEM Accuracy and Flood Zone Delineation[J]. Photogrammetric Engineering & Remote Sensing, 73(7), 793-804.

566 Samuels, P.G., 1990. Cross section location in one-dimensional models. In: White, W.R. (Ed.). International Conference on

567 River Flood Hydraulics, Wiley, Chichester, 339-350.

568 Sanders B.F., 2007. Evaluation of on-line DEMs for flood inundation modeling[J]. Advance in Water Resources, 30,

569 1831-1843.

570 Sanders, B.F., Schubert, J.E., Detwiler, R.L., 2010. ParBreZo: A parallel, unstructured grid, Godunov-type, shallow-water

571 code for high-resolution flood inundation modeling at the regional scale. Advances in Water Resources, 33,1456-1467.

572 Sanyal, J., Lu, X.X., 2006. GIS-based flood hazard mapping at different administrative scales: A case study in Gangetic West

573 Bengal, India[J].Singapore Journal of Tropical Geography, 27(2), 207-220.

574 Schubert J.E., Sanders B.F., Smith M.J., Wright N.G., 2008. Unstructured mesh generation and landcover-based resistance for

575 hydrodynamic modeling of urban flooding[J]. Adv Water Resour, 31:1603–21.

576 Schumann, G., Matgen, P., Cutler, M.E.J., Black, A., Hoffmann, L., Pfister, L., 2008. Comparison of remotely sensed water

577 stages from LiDAR, topographic contours and SRTM[J]. ISPRS Journal of Photogrammetry & Remote Sensing, 63, 283-296.

578 Sibson, R., 1981. A brief description of the natural neighbor interpolant. In: Interpreting Multivariate Data, John Wiley &

579 Sons, Chicester, 21-36.

580 Sorensen, H.R., Kjelds, J.T., Deckers, F., Waardenburg F., 1996. Application of GIS in hydrological and hydraulic modelling:

581 DLIS and MIKE Ⅱ-GIS, HydroGIS 96: Application of Geographical Information Systems in Hydrology and Water Res.

582 Management and Planning(Proceedings of the Vienna Conference, 4-1996, IAHS Publ. 235, 149-156.

583 Sukumar N., Moran B., Belikov V.V., 2001. Natural neighbour Galerkin methods[J]. International Journal for Numerical
584 Methods In Engineering, 50:1-27.
585 Tate, E., Maidment, D. 1999. Floodplain mapping using HEC-RAS and ArcView GIS, CRWR Online Report 99-1, Center for
586 Research in Water Resources, University of Texas at Austin.
587 Titus, J.G., Richman, C., 2001. Maps of lands vulnerable to sea level rise: modeled elevations along the US Atlantic and Gulf
588 coasts. Climate Research, 18, 205-228.
589 Werner, M.G.F. , 2001. Impact of Grid Size in GIS Based Flood Extent Mapping Using a 1D Flow Model[J]. Phys. Chem.
590 Earth(B), 26(7-8), 517-522.
591 Wang, Y., Colby, J.D., Mulcahy, K.A., 2002. An Efficient method for mapping flood extent in a costal floodplain using
592 Landsat TM and DEM data[J]. International Journal of Remote Sensing, 23(18), 3681-3696.
593 Zerger, A., 2002. Examining GIS decision utility for natural hazard risk modeling[J]. Environmental Modeling & Software[J].
594 17, 287-294.
595
596

Figure captions:

Figure1. The location of Dongting Lake in Yangtze River Basin.

Figure2. The location of Gongshuangcha detention basin in Dongting Lake Area.

Figure 3. 1-m-resolution DEM data for the Gongshuangcha detention basin. Coverage shown is 50×20km, Space resolution of 1m, DEM grid is 22,000 rows×51,000 columns, and file size is 4.18GB.

Figure 4 The 2D hydraulic model mesh of Gongshuangcha detention basin and its regional enlarged view.

Figure 5 The Scheme of Spatial Interpolation.

Figure 6 The Micro-topography Information of DEM.

Figure 7 Run-length Compressed Encoding of DEM.

Figure 8 Connectivity Detection between DEM Grid Cells.

Figure 9 The scheme of run-length boundary tracing and the derived flood extent.

Figure 10 The Scheme of the inundation process of Gongshuangcha detention basin in three different time periods.

Figure 11 The scheme of the inundation process on the 50th time period and its regional enlarged view.

Figure 12 The Comparison of Inundation Areas in different time periods.

Figure 13 The Comparison of Inundation Volumes in different time periods.

614 ***Figures***

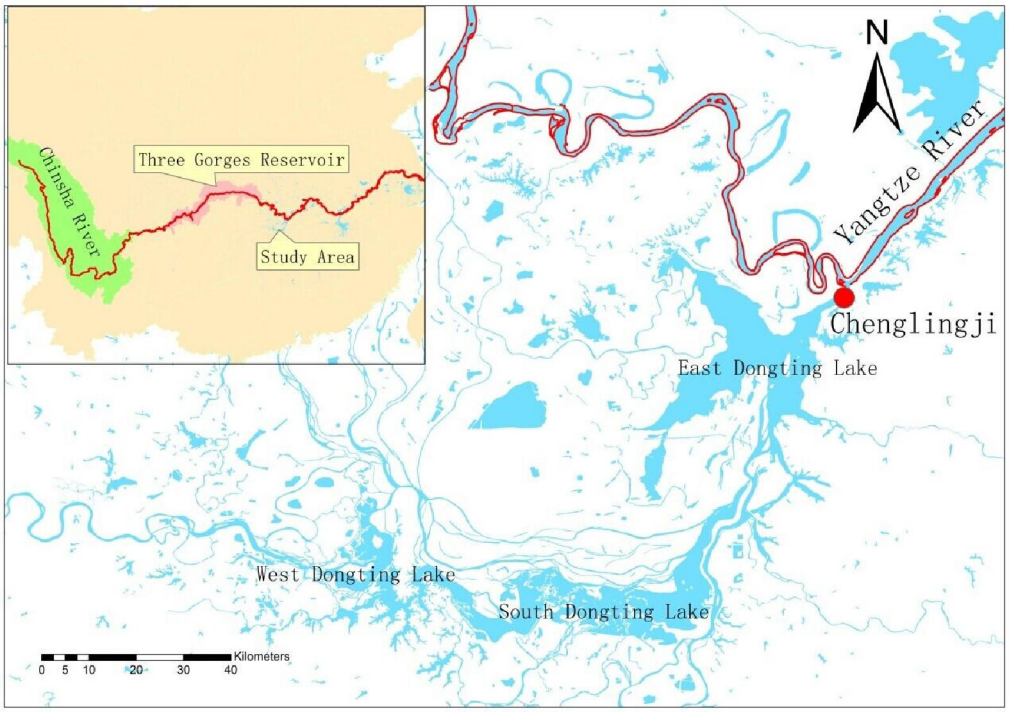

615

616 Figure1. The location of Dongting Lake in Yangtze River Basin.

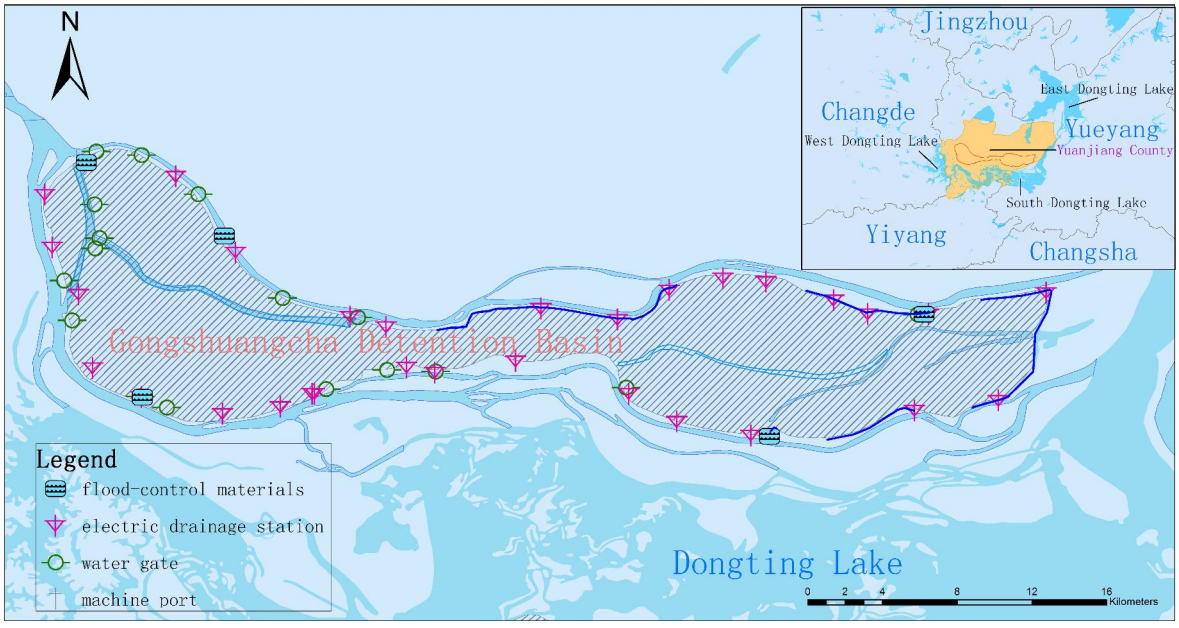

617

618 Figure2. The location of Gongshuangcha detention basin in Dongting Lake Area.

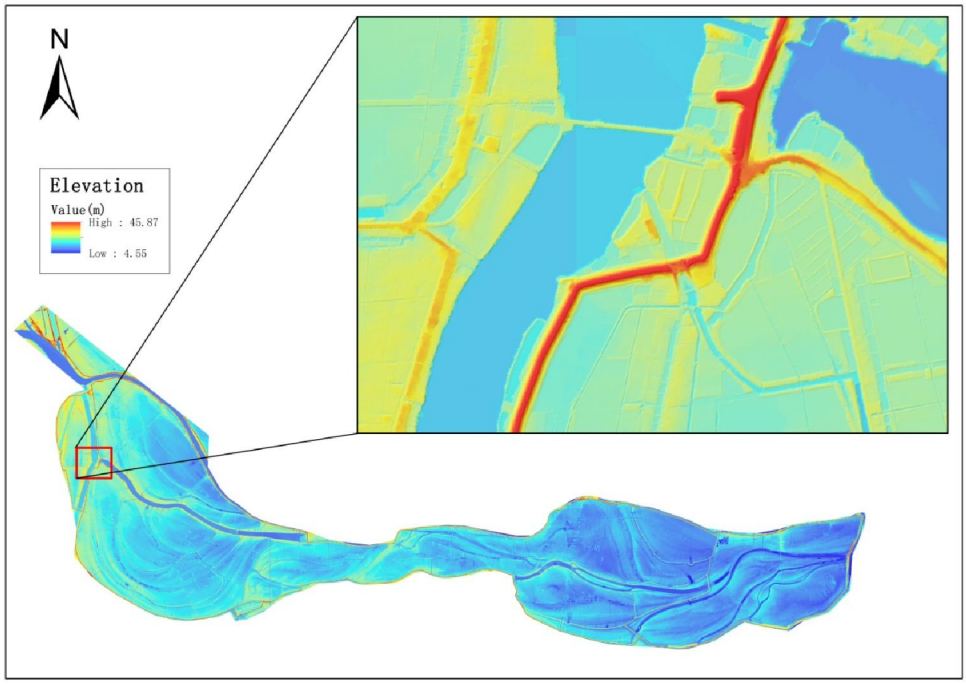

Figure 3. 1-m-resolution DEM data for the Gongshuangcha detention basin. Coverage shown is 50×20km, Space resolution of 1m, DEM grid is 22,000 rows×51,000 columns, and file size is 4.18GB.

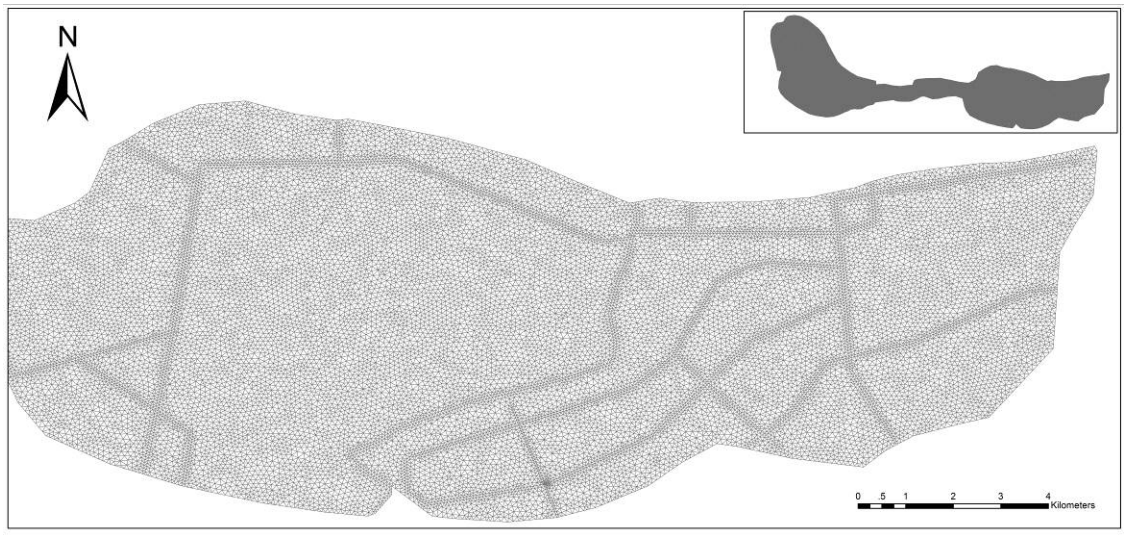

Figure 4 The 2D hydraulic model mesh of Gongshuangcha detention basin and its regional enlarged view.

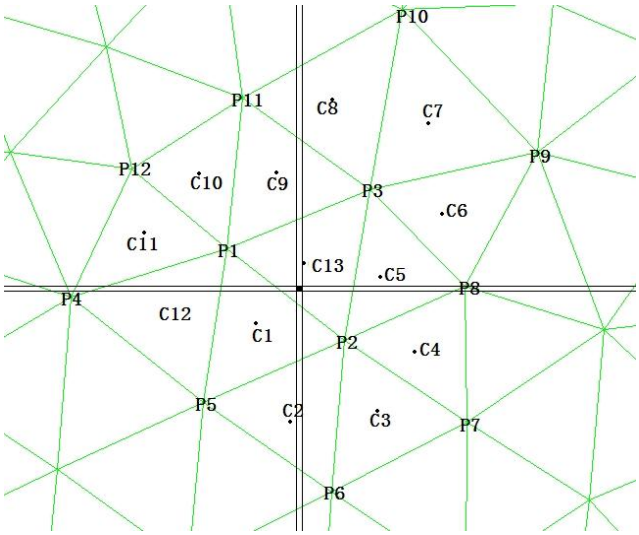

624

625 Figure 5 The Scheme of Spatial Interpolation.

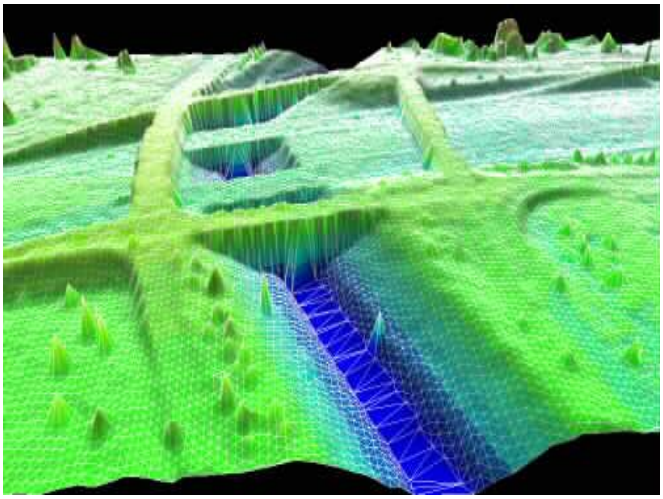

626

627 Figure 6 The Micro-topography Information of DEM.

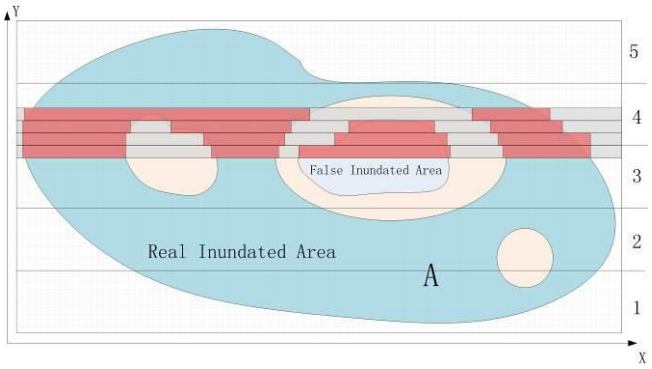

628

629 Figure 7 Run-length Compressed Encoding of DEM.

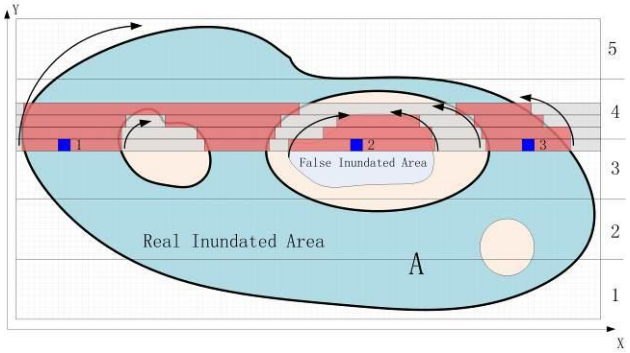

630

631 Figure 8 Connectivity Detection between DEM Grid Cells.

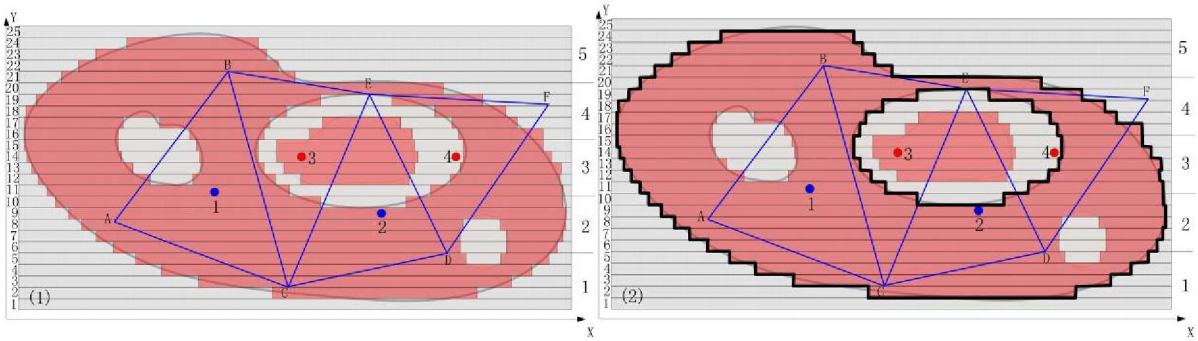

632

633

634 Figure 9 The scheme of run-length boundary tracing and the derived flood extent.

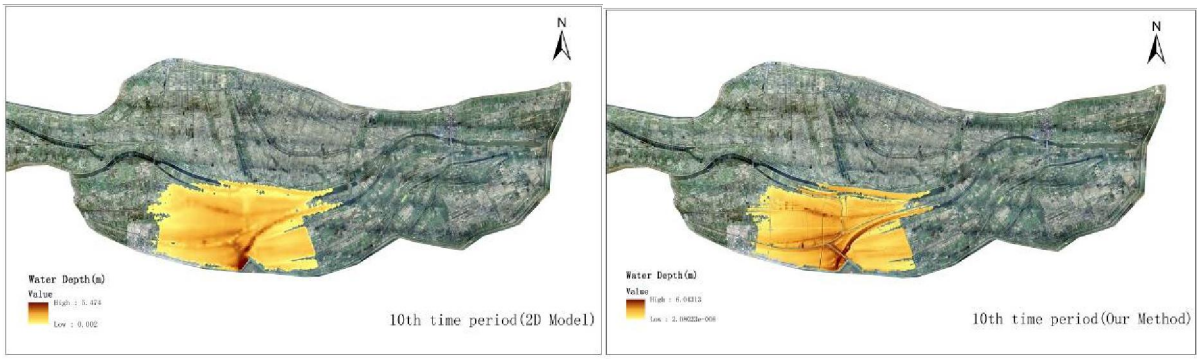

635

636

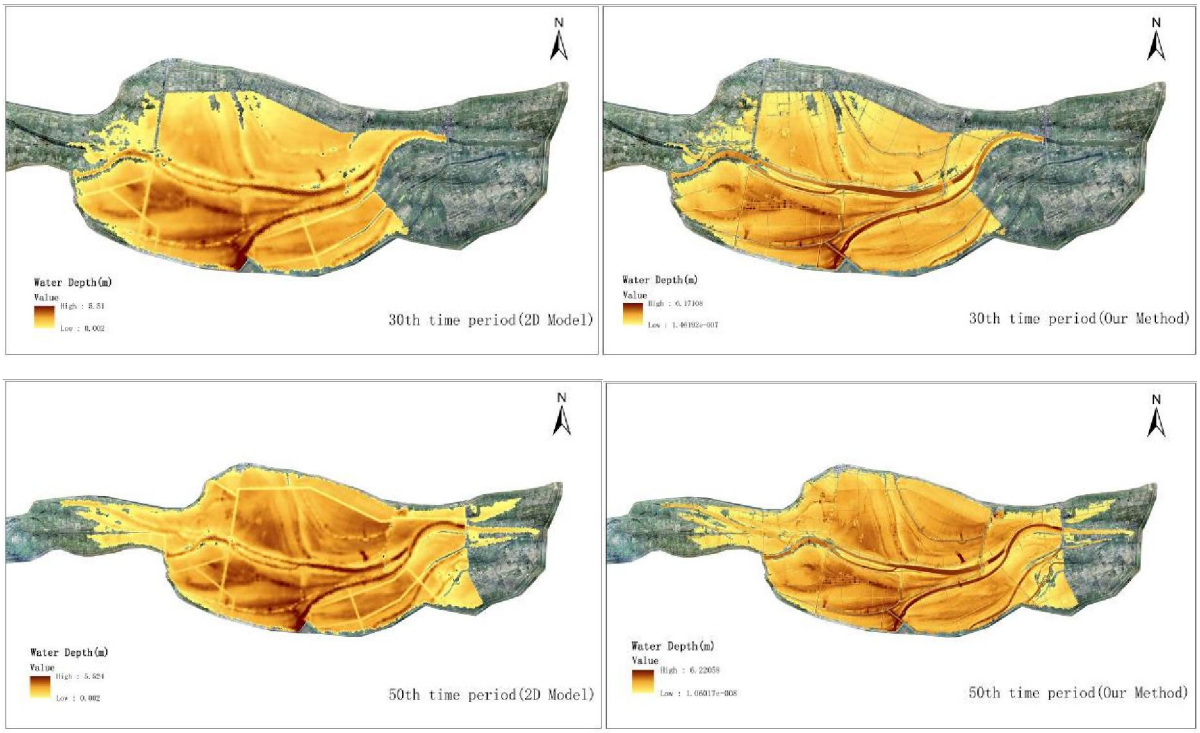

637

638 Figure 10 The Scheme of the inundation process of Gongshuangcha detention basin in three different time

639 periods

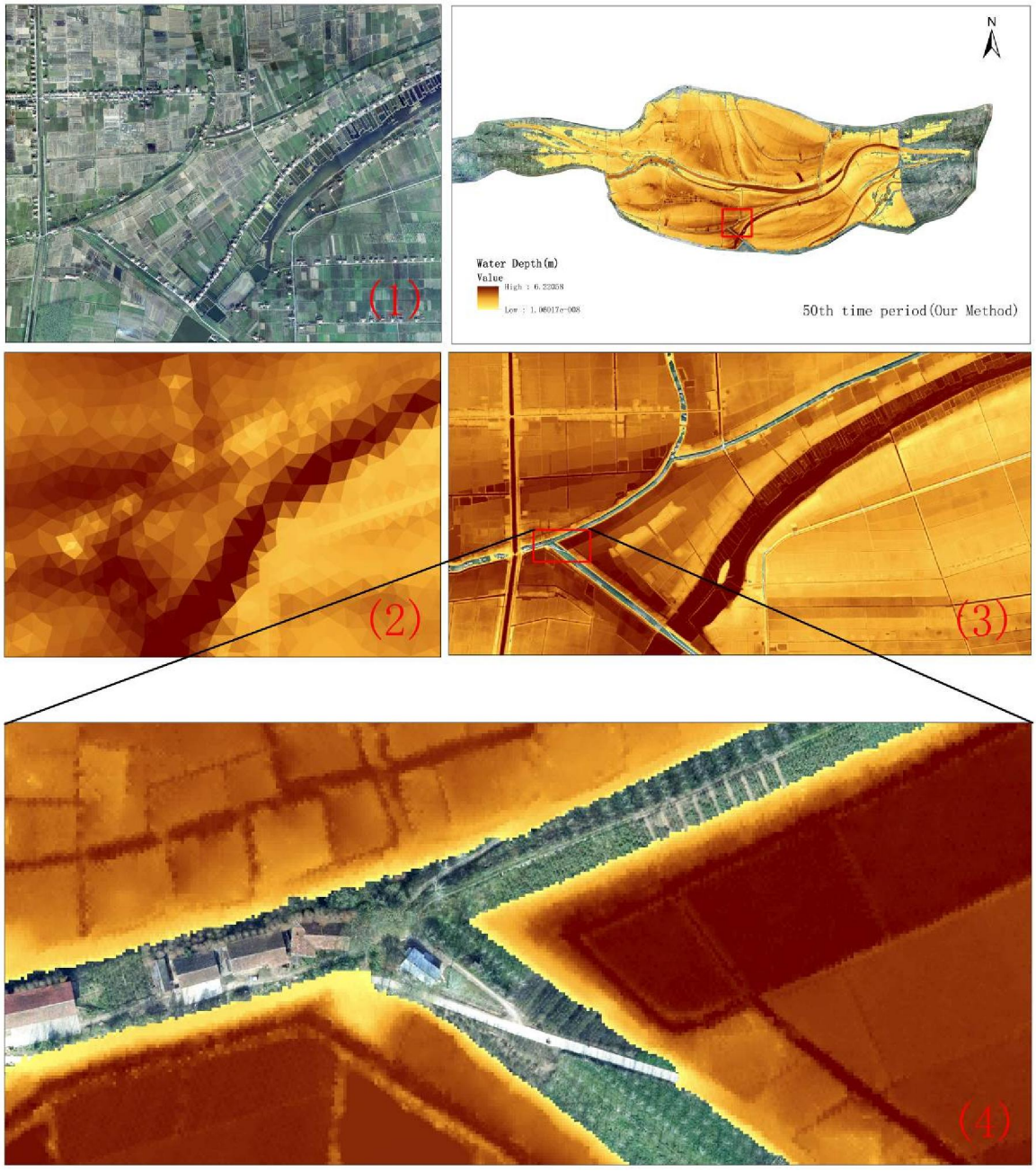

640

641 Figure 11 The scheme of the inundation process on the 50th time period and its regional enlarged view.

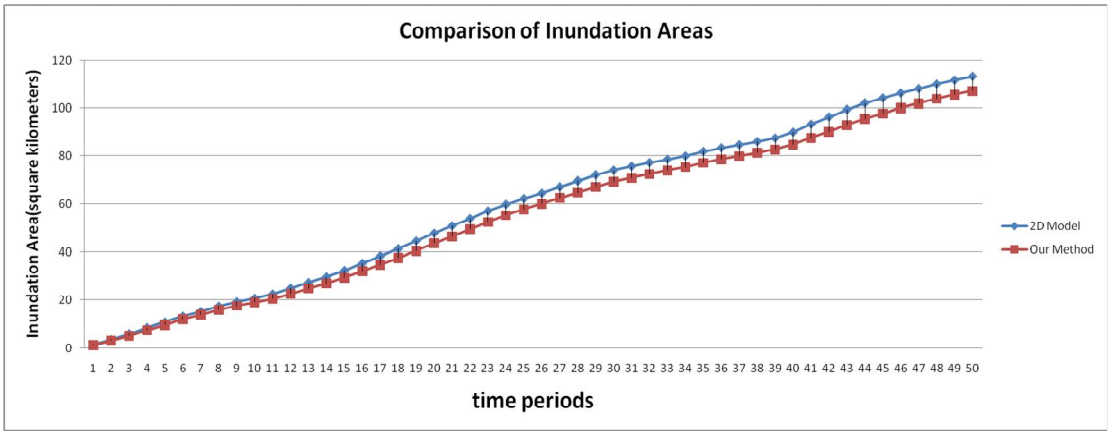

642

643 Figure 12 The Comparison of Inundation Areas in different time periods.

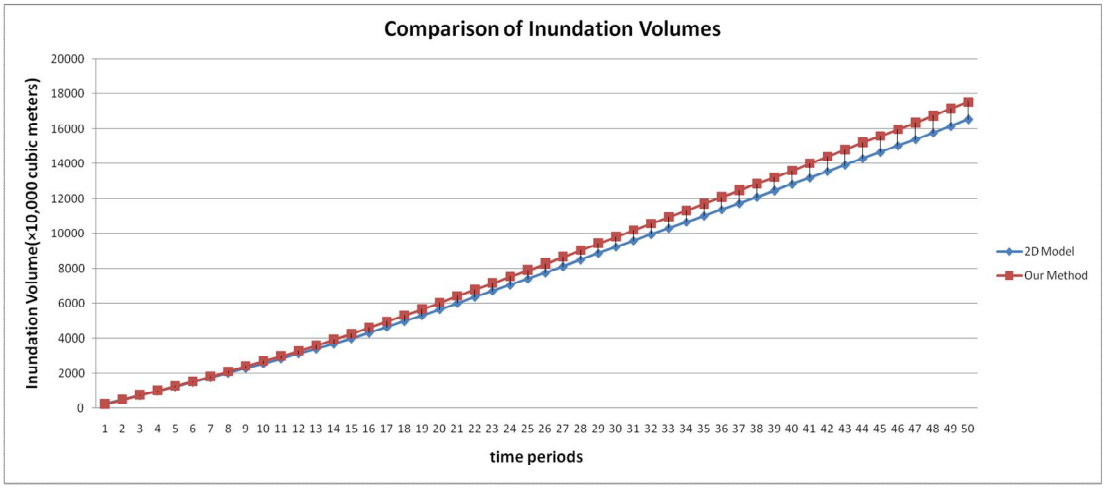

644

645 Figure 13 The Comparison of Inundation Volumes in different time periods.